SOFT ROBOTICS
Volume 00, Number 00, 2019

DOI: 10.1089/soro.2019.0005

SoRo
Soft Robotics

ORIGINAL ARTICLE

Leveraging Viscous Peeling to Create and Activate Soft Actuators and Microfluidic Devices

Lior Salem,[1] Benny Gamus,[2] Yizhar Or,[1,2] and Amir D. Gat[1,2]

Abstract

The research fields of microfluidics and soft robotics both involve complex small-scale internal channel networks, embedded within a solid structure. This study examines leveraging viscous peeling as a mechanism to create and activate soft actuators and microchannel networks, including complex elements such as valves, without the need for fabrication of structures with micron-scale internal cavities. We consider configurations composed of an internal slender structure embedded within another elastic solid. Pressurized viscous fluid is introduced into the interface between the two solids, thus peeling the two elastic structures and creating internal cavities. Since the gap between the solids is determined by the externally applied pressure, the characteristic size of the fluid network may vary with time and be much smaller than the resolution of the fabrication method. This study presents a model for the highly nonlinear elastic–viscous dynamics governing the flow and deformation of such configurations. Fabrication and experimental demonstrations of micron-scale valves and channel networks created from millimeter scale structures are presented, as well as the transient dynamics of viscous peeling-based soft actuators. The experimental data are compared with the suggested model, showing very good agreement.

Keywords: viscous flow, soft robotics, microfluidics, fluid–structure interaction

Introduction

THE TERM *VISCOUS* PEELING denotes fluid propagation into the interface between two deformable solids that are initially in contact with each other. In this study, we analytically and experimentally study viscous peeling as an approach to create and activate soft actuators and reconfigurable microchannel networks.

Fluid problems involving viscous peeling type dynamics are encountered in the context of biological flows,[1] geophysical and geological phenomena,[2–5] as well as oil and gas recovery.[6–9] The dynamics of viscous peeling are commonly governed by parabolic partial differential equations (PDEs),[5,10–13] such as the Porous Medium Equation.[14] These equations involve an inherent nonlinearity, which often yields compactly supported solutions with a nonsmoothness at a distinct propagating front (Fig. 1b), similarly to the dynamics of free-surface flows[15] and gravity currents.[16,17]

This study focuses on leveraging viscous peeling to simplify the fabrication and increase the versatility of embedded channel networks, which is relevant to lab-on-a-chip devices as well as to the emerging field of soft robotics.[18–20] By forced introduction of fluid into the interface between a slender inner solid and an external surrounding solid, viscous peeling can be used to create solid structures containing internal networks of fluid-filled channels and chambers. This eliminates the need to remove the inner core within an elastic structure to achieve internal cavities.[21–23] In addition, the nonlinear compactly supported deformation patterns evolving in such configurations allow the creation of sharp separation between activated parts and nonactivated parts of the soft actuator. Thus, multiple deformation modes can be achieved by a single geometrical configuration.

Another property of such configurations is that the internal gap between the solids, created by pressure-driven flow, is proportional to the applied fluid pressure. Thus, for sufficiently small pressures, the thickness of the channel network created in these configurations can be much smaller than the characteristic length scales of the solids before the introduction of fluid. This allows to create micron-scale fluid channels (e.g., for lab-on-a-

[1]Technion Autonomous Systems Program, Technion—Israel Institute of Technology, Haifa, Israel.
[2]Faculty of Mechanical Engineering, Technion—Israel Institute of Technology, Haifa, Israel.

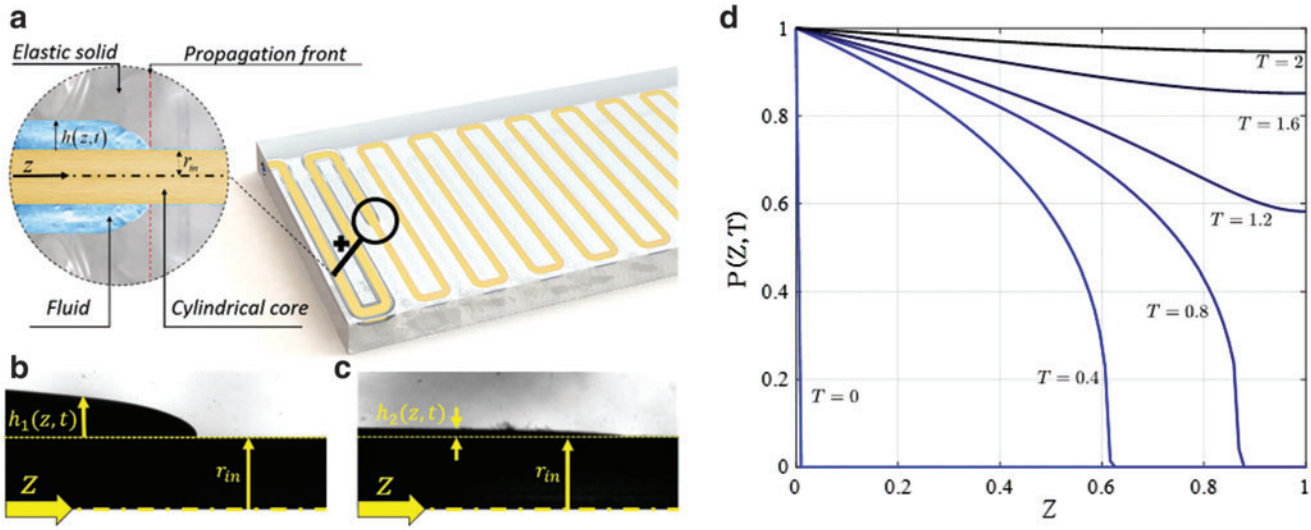

FIG. 1. Viscous peeling of an embedded slender cylinder. **(a)** Illustration of the deformation and flow propagation front due to fluid pressurization of the inlet. **(b)** Experimental figure of the propagation front shape without initial prewetting layer and **(c)** with initial prewetting layer. **(d)** Numeric solution of Equation (6) showing pressure propagation along the cylinder for various times. This solution presents nonsmoothness at a distinct propagating front, characterizing viscous peeling type dynamics. This nonsmoothness is presented for $T=0.4$ and $T=0.8$ and creates a sharp separation between pressurized and unpressurized parts of the channel. Color images are available online.

chip devices[24,25]) from millimeter-scale structures, and may pave the way to production of submicron scale fluid channels based on the same principle. In addition, this approach readily allows for the fabrication of complex geometries, which is required for microfluidic lab-on-a-chip components such as onboard valves.

The following sections model and experimentally demonstrate the incompressible viscous peeling type flows in soft actuators and microfluidic devices. The derivation of governing equations for propagation of viscous peeling is presented, as well as solutions for simplified cases. We then present experimental results of various microchannel configurations and valves, as well as the transient response of a viscous peeling-based soft actuator to fluid pressurization. These experimental measurements are compared with the theoretical model.

A Model of the Viscous Peeling Process

To understand the expected evolution of the viscous flow field and elastic deformation, this section presents the derivation and solutions of the nonlinear diffusion equation governing the process of viscous peeling.

For concreteness, we consider a slender cylinder of radius r_{in} and length l contained within a second elastic material (as shown in Fig. 1a), though other geometries can be similarly modeled. A fluid with viscosity μ and density ρ is introduced into the interface between the rigid inner cylinder and the outer elastic material. The cylindrical coordinates used are (r, z), fluid velocity is $\mathbf{u}=(v,\ w)$ in respective directions, and fluid pressure is p. Body forces are neglected and the flow is assumed to be axisymmetric.

The incompressible Newtonian fluid is governed by the Navier–Stokes equation $\rho(\partial\mathbf{u}/\partial t+\mathbf{u}\cdot\nabla\mathbf{u})=\mu\nabla^2\mathbf{u}-\nabla p$ and conservation of mass $\nabla\cdot\mathbf{u}=0$. Applying the lubrication assumptions[26] of negligible inertial effects and slender geometry ($v \ll w$, $h^* \ll l$, h^* is characteristic gap) yields the scaling of time $T=t/(\mu l^2/Er_{\text{in}}^2)$, velocity $(V,\ W)=(v/(Eh^{*2}/l\mu),\ w/(Eh^*/\mu))$, pressure $P=p/E$, and coordinates $Z=z/l$, and $R=r/r_{\text{in}}=1+\sigma_r H$ (for $\sigma_r=h^*/r_{\text{in}}$), where $H(Z,T)=h/h^*$ is the normalized thickness of the fluid layer.

Mass conservation equation in these normalized coordinates is

$$2\pi(1+\sigma_r H)\frac{\partial H}{\partial T}+\frac{\partial Q}{\partial Z}=0, \tag{1}$$

where $Q=q/(Eh^{*3}/\sigma_r\mu)$ is the normalized volumetric flux, and scaling yields $h^*=r_{\text{in}}^2/l$. Applying the standard lubrication approximation on the Navier–Stokes equations gives

$$Q(Z,T)=2\pi\int_0^H W\left(1+\sigma_r\tilde{R}\right)d\tilde{R}=\frac{\pi}{8\sigma_r^3}\frac{\partial P}{\partial Z}F(H), \tag{2}$$

where

$$F(H)\ \triangleq\ \frac{\left[(H\sigma_r+1)^2-1\right]^2}{\ln(1+\sigma_r H)}-(H\sigma_r+1)^4+1. \tag{3}$$

An additional relation between pressure P and the elastic radial deformation H is required to fully formulate the problem. Experimental results suggest a linear relation between pressure P and the change in channel area (see data in Appendix and Fig. 6). This linear relation is expressed by

$$AP=(1+\sigma_r H)^2-(1+\sigma_r H_0)^2, \tag{4}$$

where $A = a/(\pi r_i^2/E)$ (a is the dimensional constant) is a dimensionless constant of proportionality determined for each configuration and H_0 is the initial gap at $P=0$. Combining Equations (1)–(4) yields

$$8A\frac{\partial P}{\partial T} = \frac{\partial}{\partial Z}\left(\left\{\left[AP+(1+\sigma_r H_0)^2\right]^2 - 1 - 2\frac{\left[AP+(1+\sigma_r H_0)^2-1\right]^2}{\ln\left[AP+(1+\sigma_r H_0)^2\right]}\right\}\frac{\partial P}{\partial Z}\right), \quad (5)$$

which is a strongly nonlinear PDE of the normalized pressure $P(Z, T)$. Equation (5) is supplemented by the inlet pressure boundary condition $P(0, T) = P_{\text{in}}(T)$ as well as sealed boundary at $Z=1$, $\partial P/\partial Z(1, T)=0$, and an initial condition $P(Z, 0)=0$. For the general case, Equation (5) is only solvable numerically. For $H_0=0$, the zero diffusion coefficient yields propagation with a compactly supported nonsmooth front, as evident in the numerical solution presented in Figure 1d. The numeric solution was obtained through the MATLAB numeric solver PDEPE, with linear interpolation at the front point. For the limit of small characteristic gap relative to cylinder radius, $\sigma_r \ll 1$, Equation (5) is simplified to

$$\frac{\partial P}{\partial T} = \frac{A^2}{48}\frac{\partial}{\partial Z}\left(P^3\frac{\partial P}{\partial Z}\right), \quad (6)$$

which is a nonlinear diffusion equation of the form of a fourth-order porous medium equation. Such equations allow for self-similarity solutions[14,26] for a sudden release of mass at the inlet,

$$P(Z,\ T) = T^{-1/5}\left(C - \frac{3}{40}Z^2T^{-2/5}\right)_+^{1/3}, \quad (7)$$

where $(f)_+ = \max(f, 0)$ and thus the front location is obtained by setting $P=0$. Ahead of the front, trivial solution of uniform zero gauge pressure is obtained. For sudden release of mass M at the inlet given by $P(Z, 0) = 2M\delta(Z)$, where δ is Dirac's delta function, C is obtained from $\int_0^\infty P\mathrm{d}Z = M/A$.

In the following sections, steady-state solutions of Equation (5) are compared with experimental data of flows in various viscous peeling-based microchannel networks. Transient solutions Equation 7 are compared with experimental data of viscous peeling-based soft actuators.

Viscous Peeling in Microfluidic Networks and Valves

Since the gap between the solids is proportional to the fluid pressure, the characteristic thickness of the formed cavities can be much smaller than the fabrication resolution. In addition, the inner core geometry may be complex, and the creation process of the fluid-filled cavities would not require removing gas bubbles. Thus, such viscous peeling dynamics may be of interest to the fields of microfluidics and lab-on-a-chip devices. This section experimentally studies viscous peeling-based micron-sized channels and valves relevant to microfluidics, which are created from millimeter-scale structures.

Three different configurations were examined, as shown in Figure 2, and their physical properties are presented in Table 1. First, a single cylinder of length $l = 20$ mm and diameter of 0.5 mm was embedded in an elastic material with dimensions of $10\times10\times40$ mm [see Fig. 2(1.a) and additional details in Appendix]. To characterize a single viscous peeling-based microfluid channel, we measured flow rate and recorded gap thickness while controlling inlet pressure. The experimental results were compared with steady-state solution of the dimensional version of Equation (6), yielding

$$q = \frac{a^3 p_0^4}{192 r_i^2 \pi^2 \mu l} \quad (8)$$

and

$$h(z) = \left(1 - \frac{z}{l}\right)^{1/4}\frac{ap_0}{2\pi r_i}, \quad (9)$$

where $p(z=0)=p_0$ and $p(z=l)=0$ are gauge pressures at the inlet and outlet, respectively. [Steady-state solutions were obtained from Equation (6) by omitting the left hand side and integrating twice with respect to Z.]

Figure 2(1.a–1.d) shows the steady-state gap at the center of the channel, created by introducing fluid into the layer between the elastic material and solid inner cylindrical core. Figure 2(1.c) shows the experimental measurements compared with the analytic solutions for the flow rate where the parameter $a = 2.11\ \text{mm}^2/\text{MPa}$ was obtained by fitting between q and the inlet pressure p_0, based on Equation (8). Figure 2(1.d) clearly shows a micron-scale gap and compares the value of $h(z=l/2)$ obtained from Equation (9) with experimental measurements, showing good agreement with the simplified model and the calculated value of a. (We note that in the first actuation after casting, a minimal inlet pressure of ~ 10 kPa is required to separate the solids, and the presented results omit this initial actuation.)

The second configuration is a microfluidic network containing 120 parallel channels. Similarly to the single channel configuration, flow rate was measured to estimate the gap thickness within the peeling-based channels where $a = 0.63\ \text{mm}^2/\text{MPa}$ obtained by fitting to the experimental values of flow rate. The microfluidic device consists of 2 hollow inlet and outlet outer tubes that are connected with the 120 parallel inner peeling-based channels, as shown in Figure 2(2.a). Inner peeling-based channels with diameter of $\varphi_i = 0.5$ mm were fabricated, as well as hollow outer channels with diameter of $\varphi_o = 2$ mm (details regarding the fabrication process are presented in the Appendix section). The distance between adjacent channels is one channel width, and thus, based on prior results by Matia and Gat,[27] interaction between the channels can be neglected. In addition, since the hollow outer channels have a significantly smaller viscous resistance, pressure variations within the outer channels are neglected in the analytic calculation. Figure 2(2.b) compares the experimental data with the analytic solution and Figure 2(2.c) shows the estimated gap thickness. These results demonstrate the use of viscous peeling to create complex micron-scale network of fluid channels that were fabricated using low-cost millimeter-scale structures.

The third examined configuration is of an onboard microfluidic valve. Onboard valves are a rather complex yet essential element in microfluidics and lab-on-a-chip devices.[28–30] A channel and a valve were fabricated to demonstrate the capabilities of viscous peeling-based configurations and their compatibility to be integrated in lab-on-a-chip devices. Solid cylindrical core and solid tube-ring–shaped valve were

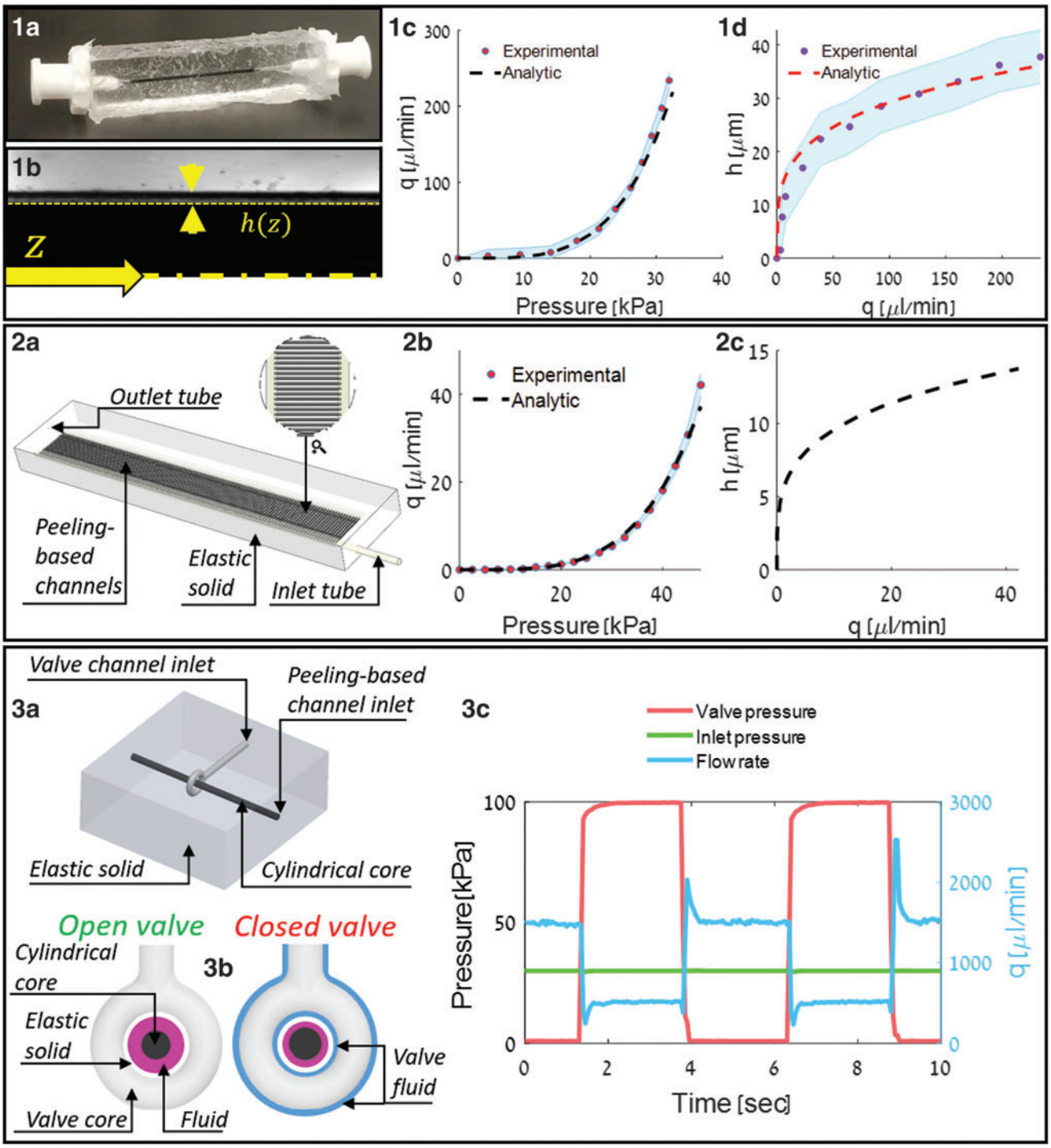

FIG. 2. Viscous peeling in microfluidic networks and valves. **(1)** Experimental illustration of leveraging viscous peeling to create a single microfluidic channel. **(1.a)** Single channel microfluidic device. **(1.b)** Gap thickness photo used to measure the gap thickness at the center of the channel. **(1.c)** Inlet pressure versus volumetric flow rate measurements. *Red dots* denote mean measured values and *black dashed lines* represent analytic calculations. *Shaded blue* region represents 1 standard deviation (SD). **(1.d)** Gap thickness at $z = L/2$ versus volumetric flow rate. *Purple dots* denote mean measured values and *red dashed lines* denote analytic calculations. *Shaded cyan* region represents 1 SD. **(2)** Experimental illustration of peeling-based channel network. **(2.a)** Illustration of the peeling-based channel network configuration. **(2.b)** Experimental measurements (*dots*) and analytic calculations (*dashed line*) of flow rate versus inlet pressure. **(2.c)** Gap thickness at $z = L/2$ versus flow rate estimated analytically from experimental values of flow rate. **(3)** Embedded peeling-based valve for microfluidic devices. **(3.a)** Illustration of the device consisting of a main peeling-based channel and a ring-shaped peeling-based valve, which are both embedded in elastic structure. **(3.b)** Cross section of peeling-based channel and ring valve. *Left figure* illustrates ''Open valve'' state, where the valve channel is unpressurized. Consequently, fluid flows without restriction along the main channel. *Right figure* illustrates partially ''closed valve'' state, where the valve channel is pressurized. Valve's fluid forces the elastic material to restrict the flow in the main channel. **(3.c)** Experimental results of flow rate through peeling-based main channel versus valve inlet pressure. Flow rate of the peeling-based main channel drops as we pressurized the valve channel. Color images are available online.

Table 1. Physical Properties of the Different Configurations

	Elastic cast dimensions	*Elastic material*	*Channel characteristics*	*Fluid*	*Relation between pressure and deformation a*
Single channel	$10\times10\times40$ mm	Sylgard184 1:25	Single cylindrical channel, $\phi=0.5$ mm	Ethanol	2.11 mm^2/MPa
Channel network	$125\times9\times45$ mm	Dragon Skin 30	120 inner cylindrical channels, $\phi_i=0.5$ mm and 2 outer channels $\phi_o=2$ mm	Water	0.63 mm^2/MPa
Valve	$50\times50\times20$ mm	Dragon Skin 30	Main channel $\phi=2$ mm, inner ring $\phi_R=4$ mm	Water	Not measured
Actuator	$125\times9\times45$ mm	Dragon Skin 30	Serpentine channel $\phi=2$ mm	Glycerin–water weight ratio 60:40	28.8 mm^2/MPa

embedded in elastomer, as shown in Figure 2(3.a). Fluid at constant pressure of 30 kPa was introduced to the channel inlet, yielding a steady-state flow in the gap between the solid cylindrical core and the elastic solid. When the valve tube-ring is pressurized, the elastic solid is compressed against the channel's cylindrical core and thus regulates the flow rate, as shown in Figure 2(3.b). Valve inlet pressure versus volumetric flux is shown in Figure 2(3.c), showing the valve's ability to regulate the flow field. This principle can be readily extended to control vast channel networks, with multiple

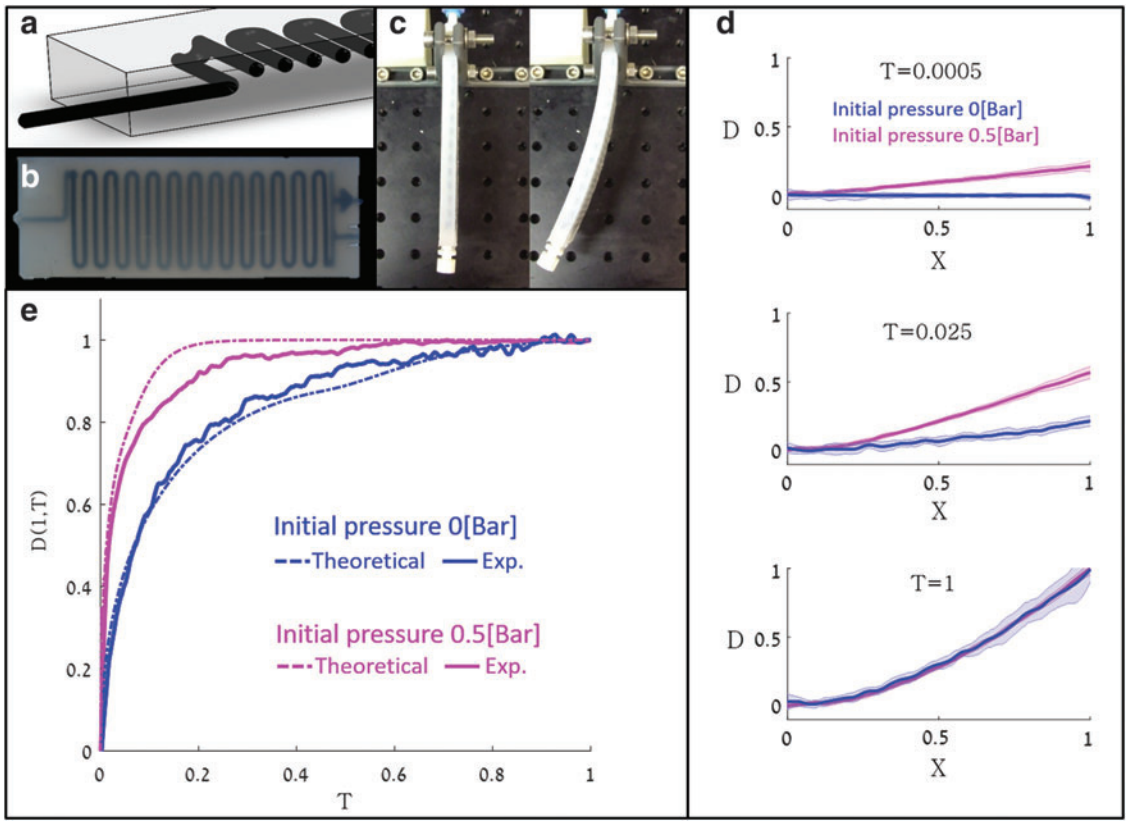

FIG. 3. Experimental illustration of a viscous peeling-based soft actuator dynamics. **(a)** Computer-aided design (CAD) image illustrating the cross section of the soft actuator. **(b)** *Top* view photo of the actuator showing the embedded serpentine channel. **(c)** Steady-state unpressurized (*left*) and pressurized (*right*) soft actuator. **(d)** Experimental results of transient actuator's deflection for step response of 0.5 Bar. We present two cases: *Blue line* denotes the deformation of an actuator without initial pressure $P_0=0$ Bar. *Magenta line* denotes the deformation of an actuator with initial pressure $P_0=0.5$ Bar, which creates initial fluid layer and increases the channel's cross section area. *Shaded areas* represent 1 SD of the experimental measurements. **(e)** Experimental measurements of the displacement of the actuator's edge $Z=1$ versus time for both cases (*solid lines*) compared with theoretical model (*dashed lines*). Color images are available online.

distributed valves. Furthermore, since the propagation of the solid deformation is governed by nonlinear diffusion Equation (5), multiple valves may be connected to a single inlet, and the actuation of the valves can be sequenced by the propagation of the peeling front between the interconnected valves (Fig. 1d).

In the following section, the transient effects of the front propagation are examined, in the context of time-dependent deformation of soft actuators.

Viscous Peeling in Soft Actuators—Transient Effects

The emerging field of soft robotics commonly employs fluid-driven soft actuators.[18–20] These soft actuators contain a complex network of interconnected embedded fluid-filled cavities. This section aims to demonstrate fabrication and activation of a viscous peeling-based soft actuator, as well as examine transient viscous peeling effects on the time-dependent deformation field of such actuators.

Figure 3a and b shows a viscous peeling-based soft actuator with an embedded serpentine core. The core, positioned at an offset from the neutral plane of the beam, is not removed from the elastomer cast. The actuator's physical properties are presented in Table 1. The actuator was mounted in clamped-free configuration, with the deflection plane perpendicular to gravity. Figure 3c shows the mounted actuator in unpressurized (left) and pressurized (right) states. The fabrication method, the experimental setup, and measurements of parameter a are described in detail in the Appendix section. Similarly to the second configuration in the previous section, the distance between adjacent channels is one channel width, and interaction between the channels is neglected, based on the results of Matia and Gat.[27]

Transient actuation of viscous peeling-based soft actuators depends on the speed of propagation of the peeling front, which is strongly affected by the initial wetting layer H_0. The value of H_0 can be modified by changing the initial pressure of the fluid. Following previous studies,[31,32] the calculation of pressure-induced deformation of a beam-shaped soft actuator can be obtained from the modified Euler–Bernoulli equation

$$\frac{\partial^2}{\partial x^2}\left[EI\left(\frac{\partial^2 d}{\partial x^2}+\lambda\varphi(x)p(x,t)\right)\right]+c\frac{\partial d}{\partial t}+\rho_s A\frac{\partial^2 d}{\partial t^2}=q, \quad (10)$$

where E is Young's modulus, I is second moment of area, d is lateral beam deformation, λ is beam slope change due to a single channel at pressure p, $\varphi(x)$ is channel density (number of channels per unit length), $p(x, t)$ is fluid pressure in channels, c is damping coefficient, ρ_S is solid density, A is cross section area, q is distributed external load, and x is an actuator–spatial longitudinal coordinate. [See Ref.[27] as well as Refs.[31,32] for detailed deviation of Equation (10).]

Two cases of transient response to a sudden increase of inlet pressure are shown in Figure 3d and e. Blue lines mark a configuration where the fluid initial pressure is $P_0=0$ Bar throughout the network and the suddenly applied inlet pressure is 0.5 Bar. In this case, the core is initially in contact with the surrounding solid. Magenta lines show a configuration where the initial pressure in the network is $P_0=0.5$ Bar and the inlet pressure is suddenly increased to 1 Bar. In this case, the initial steady pressurization creates solid deformation and a fluid film is contained between the solid core and the elastic material. Figure 3d depicts the actuator displacements (relative to the initial state) for both configurations at different times. Figure 3e shows the position of the actuator tip versus time for both configurations. The results show a significant delay between the response of the initially unpressurized configuration (blue lines, $P_0=0$ Bar) and initially pressurized configuration (magenta lines, $P_0=0.5$ Bar). This difference represents the nonlinear response of such actuators, where the initial state of the actuator significantly influences the speed of fluid front propagation, and thus the reaction speed to inlet pressurization. The experimental results were compared with the theoretical model calculated from Equations (5) and (10) and good agreement is observed.

Concluding Remarks

Leveraging flow to peel one solid from a second surrounding solid simplifies the fabrication of structures with embedded cavities, while creating a complex and highly nonlinear dynamics in response to fluid pressurization. This response is governed by a nonlinear diffusion equation relating the viscous resistance of flow within the created cavities to the fluid pressure. This study presented a model for viscous peeling dynamics, and experimentally demonstrated the properties of such configurations in the context of microfluidic networks and fluid-driven soft actuators.

The viscous–elastic interaction characterizing such structures can be utilized to extend the capabilities of lab-on-a-chip and soft actuators. For example, the distinct peeling front can be used to isolate a propagating fluid in a lab-on-a-chip device, or to clearly differentiate between activated and nonactivated regions in the context of soft robotic applications. In addition, fluid pressure can be used to create micron-scale geometries from millimeter scale structures. Although previous research on viscous peeling type mechanics was mainly examined in the context of geophysical phenomena, the application of such dynamics to lab-on-a-chip and soft robotics applications creates new fluid mechanics questions. These include viscous peeling of nonuniform internal geometries common in fluidic soft actuators (e.g., embedded sphere- or cube-shaped bladders), or viscous peeling with spatially varying properties of the surrounding elastic material.

Authors' Contributions

A.D.G. and Y.O. conceived the research subject. B.G. performed the theoretical analysis and numerical computations. L.S. conceived of the presented research, performed numerical computations, constructed the experimental setup, conducted the experiments, and analyzed the data.

Author Disclosure Statement

No competing financial interests exist.

Funding Information

This research has been supported by Israel Ministry of Science and Technology, under grant number 3-14418.

References

1. Grotberg JB, Jensen OE. Biofluid mechanics in flexible tubes. Ann Rev Fluid Mech 2004;36:121–147.
2. Michaut C. Dynamics of magmatic intrusions in the upper crust: theory and applications to laccoliths on earth and the moon. J Geophys Res 2011;116:B05205.
3. Bunger A, Cruden A. Modeling the growth of laccoliths and large mafic sills: role of magma body forces. J Geophys Res 2011;116:B02203.
4. Hewitt IJ, Balmforth NJ, De Bruyn JR. Elastic-plated gravity currents. Eur J Appl Math 2015;26:1–31.
5. Thorey C, Michaut C. Elastic-plated gravity currents with a temperature-dependent viscosity. J Fluid Mech 2016;805: 88–117.
6. Makogon Y, Holditch S, Makogon T. Natural gas-hydrates—a potential energy source for the 21st century. J Petrol Sci Eng 2007;56:14–31.
7. Lai CY, Zheng Z, Dressaire E, *et al.* Elastic relaxation of fluid-driven cracks and the resulting backflow. Phys Rev Lett 2016;117:268001.
8. Ball TV, Neufeld JA. Static and dynamic fluid-driven fracturing of adhered elastica. Phys Rev Fluids 2018;3: 074101.
9. Berhanu M, Guérin A, Courrech du Pont S, *et al.* Uplift of an elastic membrane by a viscous flow. Phys Rev E 2019; 99:043102.
10. Lister JR, Peng GG, Neufeld JA. Viscous control of peeling an elastic sheet by bending and pulling. Phys Rev Lett 2013;111:154501.
11. Elbaz SB, Gat AD. Axial creeping flow in the gap between a rigid cylinder and a concentric elastic tube. J Fluid Mech 2016;806:580–602.
12. Young YN, Stone H. Long-wave dynamics of an elastic sheet lubricated by a thin liquid film on a wetting substrate. Phys Rev Fluids 2017;2:064001.
13. Carlson A. Fluctuation assisted spreading of a fluid filled elastic blister. J Fluid Mech 2018;846:1076–1087.
14. Vázquez JL. The Porous Medium Equation: Mathematical Theory. New York: Oxford University Press, 2007.
15. Oron A, Davis SH, Bankoff SG. Long-scale evolution of thin liquid films. Rev Mod Phys 1997;69:931.
16. Huppert HE. The propagation of two-dimensional and axisymmetric viscous gravity currents over a rigid horizontal surface. J Fluid Mech 1982;121:43–58.
17. Zheng Z, Christov IC, Stone HA. Influence of heterogeneity on second-kind self-similar solutions for viscous gravity currents. J Fluid Mech 2014;747:218–246.
18. Ilievski F, Mazzeo AD, Shepherd RF, *et al*. Soft robotics for chemists. Angew Chem 2011;123:1930–1935.
19. Onal CD. System-level challenges in pressure-operated soft robotics. In: SPIE Defense+ Security. Bellingham, WA: International Society for Optics and Photonics, 2016, pp. 983627
20. Onal CD, Chen X, Whitesides GM, *et al.* (2017) Soft Mobile Robots with On-board Chemical Pressure Generation in Robotics Research. Cham, Switzerland: Springer, pp. 525–540.
21. Marchese AD, Katzschmann RK, Rus D. A recipe for soft fluidic elastomer robots. Soft Robot 2015;2:7–25.
22. Saggiomo V, Velders AH. Simple 3D printed scaffold-removal method for the fabrication of intricate microfluidic devices. Adv Sci 2015;2:1500125.
23. Esser-Kahn AP, Thakre PR, Dong H, *et al.* Three-dimensional microvascular fiber-reinforced composites. Adv Mater 2011;23:3654–3658.
24. Leslie DC, Easley CJ, Seker E, *et al.* Frequency-specific flow control in microfluidic circuits with passive elastomeric features. Nat Phys 2009;5:231.
25. Mosadegh B, Tung Y-C, Kuo C-H, *et al.* Integrated elastomeric components for autonomous regulation of sequential and oscillatory flow switching in microfluidic devices. Nat Phys 2010;6:433.
26. Leal LG. Advanced Transport Phenomena: Fluid Mechanics and Convective Transport Processes. New York: Cambridge University Press, 2007.
27. Matia Y, Gat AD. Dynamics of elastic beams with embedded fluid-filled parallel-channel networks. Soft Robot 2015;2:42–47.
28. Unger MA, Chou HP, Thorsen T, *et al*. Monolithic microfabricated valves and pumps by multilayer soft lithography. Science 2000;288:113–116.
29. Thorsen T, Maerkl SJ, Quake SR. Microfluidic large-scale integration. Science 2002;298:580–584.
30. Desai AV, Tice JD, Apblett CA, *et al*. Design considerations for electrostatic microvalves with applications in poly (dimethylsiloxane)-based microfluidics. Lab Chip 2012;12:1078–1088.
31. Matia Y, Elimelech T, Gat AD. Leveraging internal viscous flow to extend the capabilities of beam-shaped soft robotic actuators. Soft Robot 2017;4:126–134.
32. Gamus B, Salem L, Ben-Haim E, *et al*. Interaction between inertia, viscousity and elasticisy in soft robotic actuator with fluidic network. IEEE Trans Robot 2017;34:81.

Address correspondence to:
Yizhar Or
Faculty of Mechanical Engineering
Technion—Israel Institute of Technology
Technion City
Haifa 3200003
Israel

E-mail: izi@technion.ac.il

Amir D. Gat
Faculty of Mechanical Engineering
Technion—Israel Institute of Technology
Dan Kahn 409
Technion City
Haifa 3200003
Israel

E-mail: amirgat@technion.ac.il

(*Appendix follows* →)

Appendix

Fabrication and Experimental Setup of Microfluidic Networks and Valves

The single peeling-based channel shown in Figure 2(1.a–1.d) was fabricated from ABS fibers through a BCN Sigma 3D printer. The printed cylinder was embedded in Sylgard184 (1:25 ratio) and cured in room temperature for 1 week. Luer connectors were attached with Sil-Poxy—SmoothOn, Inc. The pressure controller was connected to water-filled reservoir connected to the elastic device. We measured inlet pressure (Baumer PBMN B22) and flow rate (CORI-FLOW™; Bronkhorst) while recording the gap thickness through microscope (Nikon eclipse Ti, ANDOR Clara, lumencor Mira).

The network of peeling-based microfluidic channels shown in Figure 2(2.a–2.c) was fabricated using dual-extrusion BCN Sigma 3D printer. In a single print job, inner peeling-based channels were made from polylactic acid (PLA) fibers, and outer channels were made from polyvinyl alcohol (PVA) fibers. The single printed part was embedded in Dragon Skin 30, Smooth-On, Inc. Next, only PVA outer channels were dissolved using warm water (40°C) creating cavities along the outer channels. The experiment setup is similar to the single channel configuration, excluding a different flow rate indicator (Elveflow MFS5).

The embedded peeling-based valve shown in Figure 2(3.a–3.c) was fabricated using 3D printing similarly to the previous configurations. The device consists of two solid parts and an elastic cast. The main peeling-based channel and the ring-shaped peeling-based valve were made from PLA fibers. The diameter of the main channel is 2 mm, the diameter of the valve's channel is 2 mm where the inner diameter of the ring is 4 mm. The parts are located such that the cylindrical main channel passes through the ring and is concentric to it. The parts were embedded in $50 \times 50 \times 20$ mm elastomer structure (Dragon Skin 30). Two pressure regulator channels (Elveflow OB1) were connected through reservoirs to the peeling-based main channel and the valve's channel inlets. The inlet pressure of the main channel was held constant and its outlet was subjected to atmospheric pressure. The valve was regulated by controlling the valve's channel inlet pressure. The experimental setup utilized the Elveflow MFS5 flow rate indicator and the Baumer PBMN B22 pressure sensor.

Fabrication and Experimental Setup of Viscous Peeling-Based Soft Actuator

The soft actuator shown in Figure 3(a–c) was fabricated by embedding a 3D printed core (PLA; BCN Sigma) in a serpentine geometry into an elastomer cast (DragonSkin30; Smooth-On, Inc.) as shown in Figure 4. The embedded serpentine core is positioned at an offset from the neutral plane of the beam. Luer connectors were glued using silicone rubber adhesive (Sil-Poxy; Smooth-On, Inc.). Actuator's geometry and physical properties are length $l_s = 125$ mm, height $h_s = 9$ mm, width $b_s = 45$ mm, Young's modulus $E = 0.97$ MPa, density $\rho = 1120$ kg/m^3, and damping ratio $\zeta = 1.46$. Inner core properties are length $l_c = 1350$ mm, radius $r_c = 1$ mm, offset of 2.5 mm from the neutral plane, and the

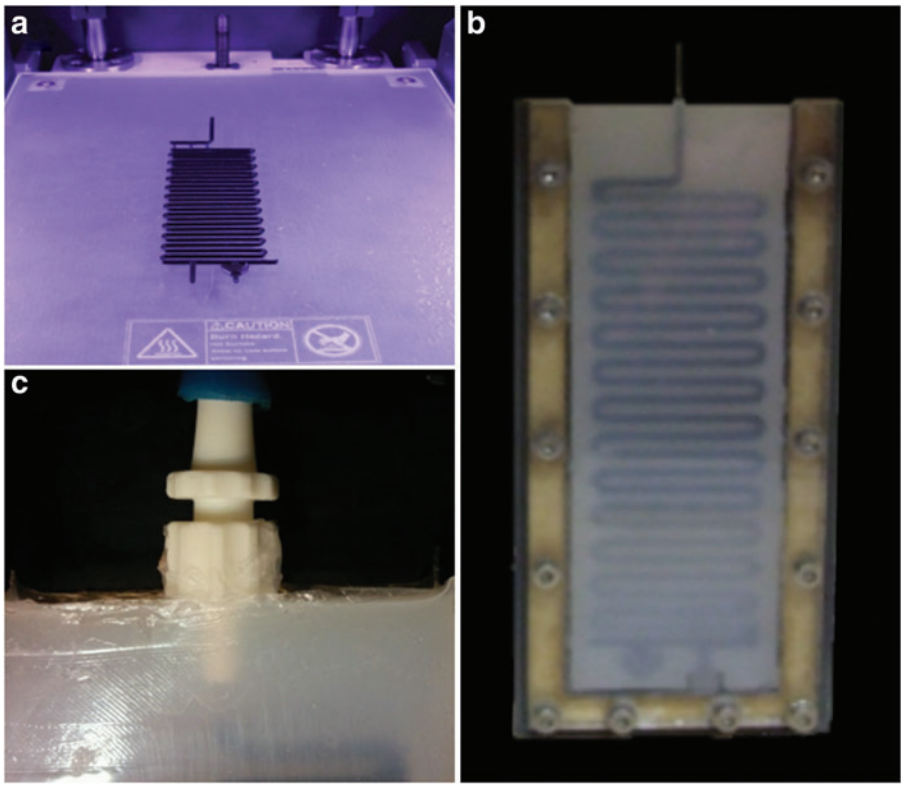

FIG. 4. Fabrication process of a viscous peeling-based soft actuator. **(a)** 3D printed PLA core. **(b)** Elastomer cast around 3D solid core, which remains in the elastomer. **(c)** Attaching inlet luer connector using Sil-Poxy. PLA, polylactic acid. Color images are available online.

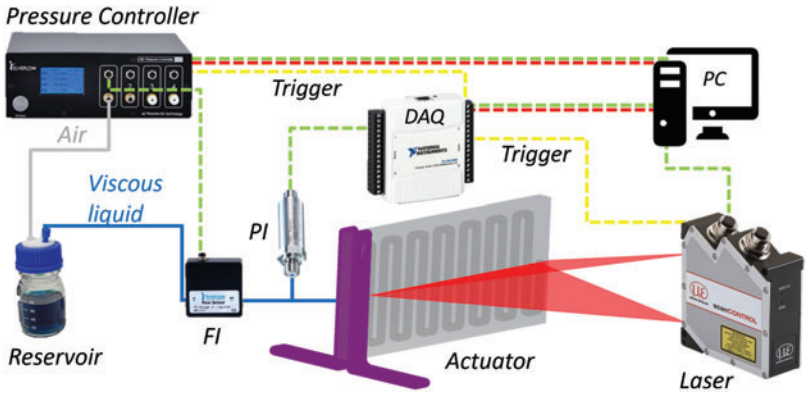

FIG. 5. Experimental setup for transient deformation measurements of a viscous peeling-based soft actuator. A pressure controller (Elveflow OB1) is connected to a fluid-filled reservoir and sets the inlet pressure. Laser profilometer (MicroEpsilon LLT 2650-100) captures and records the time-dependent deformation of the actuator. Flow rate indicator (Elveflow MFS5) and pressure sensor (Baumer PBMN B22 through NI USB-6009 DAQ) record the flow rate and inlet pressure, respectively. *Solid lines* represent fluidic tube. *Dashed lines* represent data lines, where *red* represents input, *green* represents output, and *yellow* represents trigger. Color images are available online.

serpentine channel is composed of $n = 26$ parallel channels, where $a = 28.8\ \text{mm}^2/\text{MPa}$ obtained by calibration experiment detailed in the Appendix. The actuator was mounted in clamped-free configuration, with the deflection plane perpendicular to gravity. A pressure controller (Elveflow OB1) was connected to reservoir filled with 60:40 weight ratio glycerin–water mixture. The reservoir outlet was connected to a flow rate sensor (Elveflow MFS5), pressure sensor (Baumer PBMN B22), and to actuator's inlet. A laser profilometer beam (MicroEpsilon LLT 2650-100) was placed in front of the deflection plane to measure its transverse deformation relative to its contour at rest. The laser was positioned 300 mm from the actuator and provided 640 spatial sample points. An electric trigger was used to simultaneously activate the pressure controller, flow rate indicator, pressure indicator, and the laser profilometer. The experimental setup is shown in Figure 5.

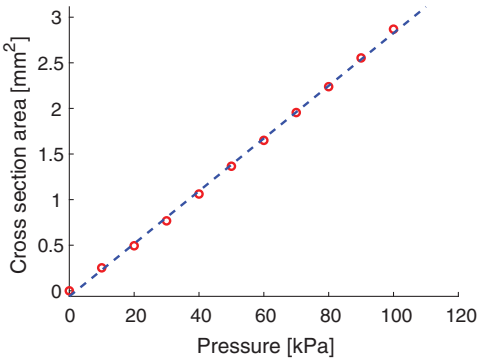

FIG. 6. Experimental steady-state measurements of fluidic pressure versus variation in cross-sectional area. Cross-sectional area variation is computed by $\Delta v/l$, where Δv and the total fluidic volume and l is the total length of the serpentine channel. *Red circles* denotes measured values and *blue dashed line* denotes a linear relation. The geometrical and physical properties of the configuration are described in the text. Color images are available online.

Experimental Relation Between Fluidic Pressure and Elastic Deformation

The governing lubrication Equations (1)–(3) require an additional relation between the fluidic pressure P and the elastic deformation H. This relation was estimated experimentally by introducing a pressurized fluid into the gap between a serpentine solid channel and the surrounding elastic material, at pressure range of 0 to 100 kPa. The configuration's fabrication process, geometrical and physical properties are identical to those described in the previous subsection. For each fluidic pressure, the fluid volume added between the solids was measured visually by a measuring cylinder.

The variation in cross-sectional area is thus obtained by $\Delta v/l$, where Δv is the total fluidic volume and l is the total length of the serpentine channel. Assuming a circular cross section, the relation between the radial deformation H and the fluidic pressure P can thus be obtained. The experimental measurements suggest a linear relation between pressure P and the change in cross-sectional area, given by

$$ap = \pi(r_i + h)^2 - \pi(r_i + h_0)^2, \tag{11}$$

as shown in Figure 6, where a is the coefficient of proportionality, r_i is the inner cylinder radius, h is channel thickness at pressure p, and h_0 is the channel thickness at $p = 0$. In dimensionless form, this relation is given by $AP = (1 + \sigma_r H)^2 - (1 + \sigma_r H_0)^2$, where $A = a/(\pi r_i^2/E)$. (For sufficiently small P, this relation can be simplified further to a linear relation between P and H.)